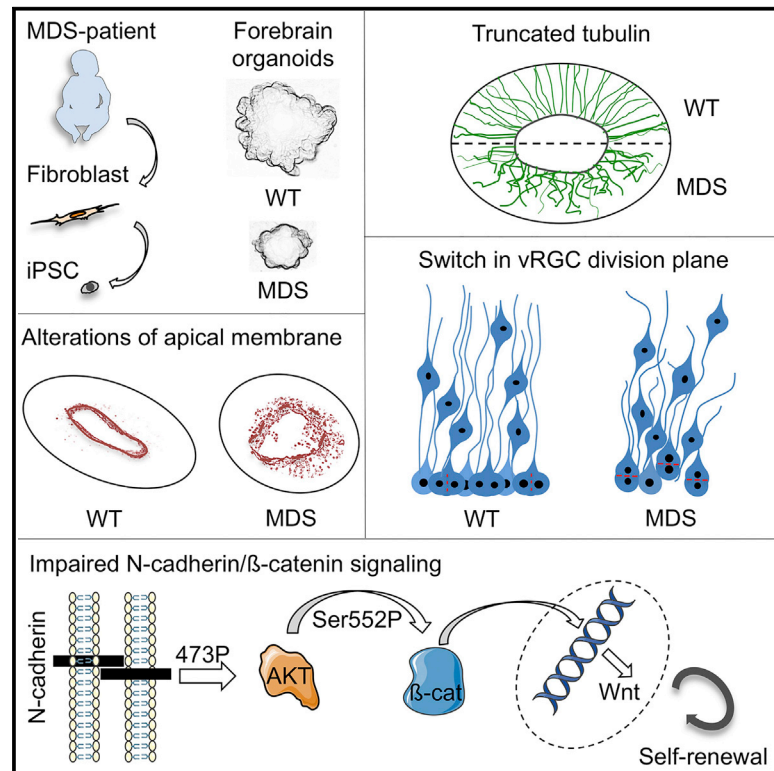


## An Organoid-Based Model of Cortical Development Identifies Non-Cell-Autonomous Defects in Wnt Signaling Contributing to Miller-Dieker Syndrome

### Graphical Abstract



### Authors

Vira Iefremova, George Manikakis, Olivia Krefft, ..., Franz-Josef Müller, Philipp Koch, Julia Ladewig

### Correspondence

philipp.koch@uni-bonn.de (P.K.),  
jladewig@uni-bonn.de (J.L.)

### In Brief

Using Miller-Dieker-syndrome-specific iPSC-derived forebrain-type organoid cultures, Iefremova et al. find that a disturbance of cortical niche signaling leads to alterations in N-cadherin/ $\beta$ -catenin signaling that result in a non-cell-autonomous expansion defect of ventricular zone radial glia cells.

### Highlights

- Homogeneous forebrain-type organoids reflect early cortical development in vitro
- MDS-derived organoids show reduced expansion rate caused by premature neurogenesis
- MDS-derived organoids exhibit alterations in cortical niche architecture
- Niche disruption leads to a non-cell-autonomous disturbance of  $\beta$ -catenin signaling



# An Organoid-Based Model of Cortical Development Identifies Non-Cell-Autonomous Defects in Wnt Signaling Contributing to Miller-Dieker Syndrome

Vira Iefremova,<sup>1,3</sup> George Manikakis,<sup>1,3</sup> Olivia Krefft,<sup>1</sup> Ammar Jabali,<sup>1</sup> Kevin Weynans,<sup>1</sup> Ruven Wilkens,<sup>1</sup> Fabio Marsoner,<sup>1</sup> Björn Brändl,<sup>2</sup> Franz-Josef Müller,<sup>2</sup> Philipp Koch,<sup>1,\*</sup> and Julia Ladewig<sup>1,4,\*</sup>

<sup>1</sup>Institute of Reconstructive Neurobiology, University of Bonn, Bonn 53127, Germany

<sup>2</sup>Department of Psychiatry and Psychotherapy, University Hospital Schleswig Holstein, Kiel 24105, Germany

<sup>3</sup>Co-first author

<sup>4</sup>Lead Contact

\*Correspondence: [philipp.koch@uni-bonn.de](mailto:philipp.koch@uni-bonn.de) (P.K.), [jladewig@uni-bonn.de](mailto:jladewig@uni-bonn.de) (J.L.)

<http://dx.doi.org/10.1016/j.celrep.2017.03.047>

## SUMMARY

Miller-Dieker syndrome (MDS) is caused by a heterozygous deletion of chromosome 17p13.3 involving the genes *LIS1* and *YWHAE* (coding for 14.3.3 $\epsilon$ ) and leads to malformations during cortical development. Here, we used patient-specific forebrain-type organoids to investigate pathological changes associated with MDS. Patient-derived organoids are significantly reduced in size, a change accompanied by a switch from symmetric to asymmetric cell division of ventricular zone radial glia cells (vRGCs). Alterations in microtubule network organization in vRGCs and a disruption of cortical niche architecture, including altered expression of cell adhesion molecules, are also observed. These phenotypic changes lead to a non-cell-autonomous disturbance of the N-cadherin/ $\beta$ -catenin signaling axis. Reinstalling active  $\beta$ -catenin signaling rescues division modes and ameliorates growth defects. Our data define the role of *LIS1* and 14.3.3 $\epsilon$  in maintaining the cortical niche and highlight the utility of organoid-based systems for modeling complex cell-cell interactions in vitro.

## INTRODUCTION

The evolutionary increase in the size of the human cerebral cortex is thought to be responsible for the extraordinary cognitive abilities of humans. This evolution was achieved by increased expansion of the surface area accompanied by the formation of gyri and sulci. Lissencephaly represents a malformation of cortical development (MCD) connected with neuronal disorganization and absent or abnormal gyrification (Francis et al., 2006). Heterozygous deletions or mutations of *LIS1* constitute the most common cause of lissencephaly in humans (Kato and Dobyns, 2003). The *LIS1* protein is a component of an intracellular multi-protein complex including NDEL1 and 14.3.3 $\epsilon$ , which is essential

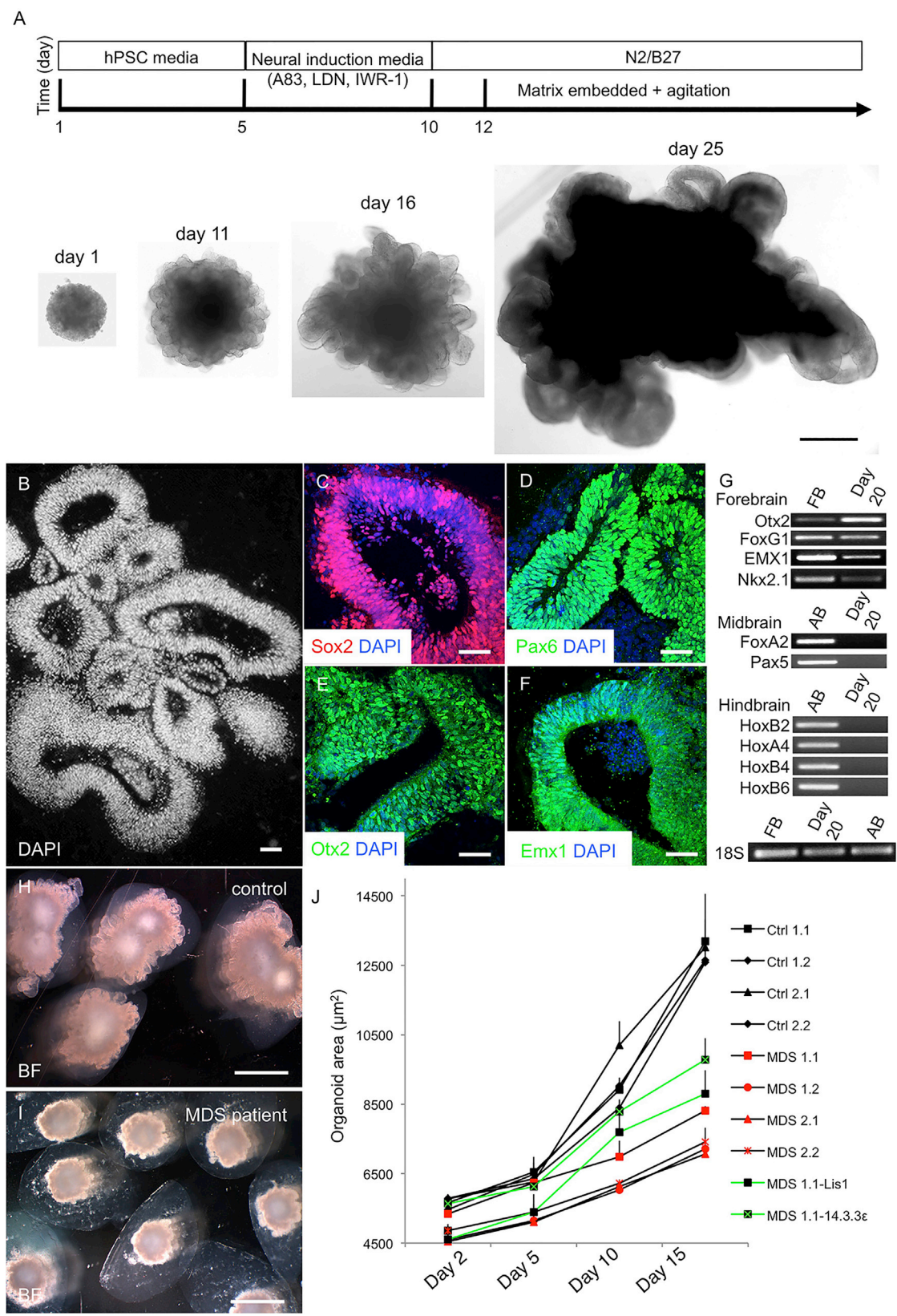
for the regulation of cytoplasmic dynein, centrosomal protein localization, and microtubule dynamics (Wynshaw-Boris, 2007). Traditionally, *LIS1*-associated lissencephalies were considered as isolated neuronal migration defects (Moon and Wynshaw-Boris, 2013). More recent data, however, highlight a role of the *LIS1*/NDEL1/14.3.3 $\epsilon$  complex in the proliferation of radial glia cells (RGCs) (Bi et al., 2009; Tsai et al., 2005; Yingling et al., 2008). In Miller-Dieker syndrome (MDS), two components of the *LIS1*/NDEL1/14.3.3 $\epsilon$  complex (*LIS1* and 14.3.3 $\epsilon$ ) are affected resulting in increased structural alterations of the cortical architecture compared to isolated lissencephaly. Although mouse models have confirmed a role of the *LIS1*/NDEL1/14.3.3 $\epsilon$  complex in several cellular processes, they failed to recapitulate the severity of the human phenotype (Toyo-oka et al., 2003; Yingling et al., 2008). Recent progress in modeling human brain development in vitro uses the capacity of pluripotent stem cells (PSCs) to self-organize into organoids. Brain organoids contain different neural and neuronal subtypes, which spatially organize similarly to the developing human brain and faithfully recapitulate developmental gene expression patterns (Camp et al., 2015; Kadoshima et al., 2013; Lancaster et al., 2013; Mariani et al., 2015; Qian et al., 2016).

In this study, we used a standardized forebrain organoid protocol to model changes associated with MDS in vitro. We observed a reduced expansion rate of MDS organoids associated with an unexpected switch of the division mode of ventricular radial glia cells (vRGCs, or also called apical radial glia) from symmetric to asymmetric cell division. Furthermore, we identified a unrecognized mechanism of how a deficiency of the *LIS1*/NDEL1/14.3.3 $\epsilon$  complex converges into an impairment of ventricular zone niche signaling and cell-fate control via the N-cadherin/ $\beta$ -catenin signaling axis in a non-cell-autonomous fashion.

## RESULTS

### Generation of Standardized iPSC-Derived Forebrain-type Organoids

We generated induced pluripotent stem cells (iPSCs) from two patients with MDS and two age- and gender-matched controls



(legend on next page)

(two clones each; characterization of iPSCs is illustrated in [Figures S1A–S1G](#) and [Table S1](#)). The MDS patient-specific heterozygous deletion of chromosome 17p13.3 was confirmed by SNP genotyping and reduced expression of *LIS1* and *YWHAE* by qRT-PCR ([Figures S1G–S1I](#)). As isogenic controls and to address the specific role of *LIS1* and 14.3.3 $\epsilon$  in MDS, we generated *LIS1* and 14.3.3 $\epsilon$  rescue cell lines by introducing a doxycycline-inducible *LIS1* (MDS-LIS1) or *YWHAE* (MDS-14.3.3 $\epsilon$ ) into the human *AAVS1* locus of MDS iPSCs. Addition of doxycycline increased the expression of *LIS1* or *YWHAE* back to expression levels comparable to control cultures ([Figures S1J](#) and [S1K](#)).

We next generated standardized organoids of forebrain identity by combining guided differentiation of iPSCs into anterior neuroectoderm using SMAD and Wnt inhibition ([Kadoshima et al., 2013](#)) with matrix embedding to promote continuous neuroepithelium formation ([Lancaster et al., 2013](#)). To increase oxygen exchange, cultures were maintained under agitating conditions ([Lancaster et al., 2013](#); [Qian et al., 2016](#)) (protocol outlined in [Figure 1A](#)). Control iPSC-derived organoids consistently increased in size over time while forming large neuroepithelial loops ([Figures 1A](#) and [S2A–S2C](#)). Immunocytochemical analysis revealed that at day  $20 \pm 2$  organoids consist of stratified neuroepithelial loops expressing the neural progenitor marker Sox2 and the forebrain markers Pax6, Otx2, and Emx1, indicating a dorsal telencephalic identity ([Figures 1B–1F](#)). Few loops stained positive for the ventral forebrain progenitor-associated transcription factor Nkx2.1 ([Figure S2D](#)). Dividing cells expressing phosphorylated vimentin (p-vimentin) locate at the apical surface of the cortical loops ([Figure S2E](#)). RT-PCR investigating typical forebrain, midbrain, and hindbrain markers confirmed homogeneous forebrain identity of the organoids ([Figures 1G](#) and [S2F](#)). At later time points (day  $35 \pm 2$  days), loops developed into a more complex organized and stratified cortical tissue with densely packed Sox2-positive cortical progenitors preferentially locating on the inside/apical surface of the organoids and separating from  $\beta$ III-tubulin-positive neurons at the outside/basal surface of the structures, reminiscent of a ventricular zone (VZ) and an initial cortical plate (CP), respectively ([Figure S2G](#)). Tbr2-positive intermediate progenitors (IPs) were located in a subventricular zone (SVZ)-like transition zone between the VZ- and the CP-like structure ([Figure S2H](#)). Sox2-positive progenitors were also observed in the SVZ-like area potentially representing outer radial glia (oRG or also called basal radial glia; [Figure S2I](#)). Within the CP-like area, initial cortical layering could be observed ([Figures S2J–S2L](#)).

### Premature Neurogenesis Leads to Reduced Expansion of MDS Patient-Specific Organoids

The forebrain organoid protocol was then applied to MDS patient-derived iPSCs. Similar to control organoids, MDS orga-

noids consistently produced Sox2-positive stratified loops expressing forebrain-specific transcription factors such as Otx2, Pax6, FoxG1, and Emx1, while typical mid- and hindbrain markers were undetectable ([Figures S2F](#) and [S2M–S2Q](#)). However, in contrast to control organoids, MDS-derived organoids were significantly smaller in size and showed significantly reduced expansion rates ([Figures 1H–1J](#) and [S2R–S2S](#); [Table S2](#)). Re-expression of *LIS1* or 14.3.3 $\epsilon$  resulted in a partial rescue of these expansion deficits ([Figure 1J](#); [Table S2](#)). We further assessed the architecture of the neuroepithelial loops by determining the length of the apical and basal membrane, the diameter of the loops as well as the size of the ventricle-like area, the total loop area, and the loop tissue area in patient- and control-derived organoids. Here, we observed a significant reduction in all parameters in MDS-derived organoids compared to controls with re-expression of *LIS1* or 14.3.3 $\epsilon$  leading to a partial rescue toward the wild-type situation ([Figures 2A–2D](#) and [S3](#)). This phenotype is in line with autopsy examinations of MDS patients' brains showing severe reduction in total brain size ([Sheen et al., 2006](#)).

The reduced brain size of MDS patients as well as the changes we observed in our model might arise from impairments in several developmental processes. We first investigated apoptotic cell death in neuroepithelial progenitors as a potential underlying mechanism of the reduced size and expansion rates of MDS organoids by quantifying cleaved (active) caspase-3 at several time points. This analysis revealed that apoptotic cell death is rare at all time points investigated and that there is no significant difference in the number of apoptotic neuroepithelial progenitors when comparing patients with controls ([Figures S4A](#) and [S4B](#)). Another potential mechanism postulated is that a disruption of the *LIS1*/NDEL1/14.3.3 $\epsilon$  complex results in a reduction and weakening of astral microtubules and decreased plus-end stability of cortical microtubules leading to alterations of the microtubule array. As a consequence, precise control of vRGCs' mitotic spindle orientation and plane of cleavage is disturbed resulting in a randomized spindle orientation with an increase in oblique cleavage planes ([Yingling et al., 2008](#)). Indeed, we observed severe alterations in the organization of MDS vRGCs' microtubule networks. Whereas in control organoids, the vRGC microtubule network (stained by acetylated  $\alpha$ -tubulin) extends the entire distance from the apical to the basal side, MDS vRGCs' microtubules appear truncated and show a significant reduction of extensions toward the basal membrane ([Figures 2E–2G](#), [S4C](#), and [S4D](#)). In MDS-LIS1 and MDS-14.3.3 $\epsilon$  rescue organoids, microtubule networks still seemed to be altered but showed a more pronounced expansion of acetylated  $\alpha$ -tubulin toward the basal surface ([Figures 2G](#), [S4O](#), and [S4P](#)).

### Figure 1. Reduced Size and Expansion Rates of MDS Patient-Derived Forebrain-type Organoids

- (A) Schematic overview of the organoid protocol and representative images. Scale bar, 500  $\mu$ m.  
 (B–F) Immunocytochemical characterization of organoids at day  $20 \pm 2$ . Organoids organize in multiple neuroepithelial loops (B). Neuroepithelial cells express Sox2 (C), Pax6 (D), Otx2 (E), and Emx1 (F). Scale bars, 50  $\mu$ m.  
 (G) RT-PCR analysis for region-specific transcription factors at day 20. FB, fetal brain control; AB, adult brain control.  
 (H and I) Representative bright-field images of control- (H) and MDS patient- (I) derived organoids at day 25. Scale bars, 2.5 mm.  
 (J) Expansion rates of control- ( $n = 30$  for each clone), MDS- ( $n = 30$  for each clone), MDS-LIS1- ( $n = 20$ ), and MDS-14.3.3 $\epsilon$ - ( $n = 20$ ) derived organoids. Depicted is the organoid area in  $\mu$ m<sup>2</sup> at days 2, 5, 10, and 15. Error bars,  $\pm$ SD.

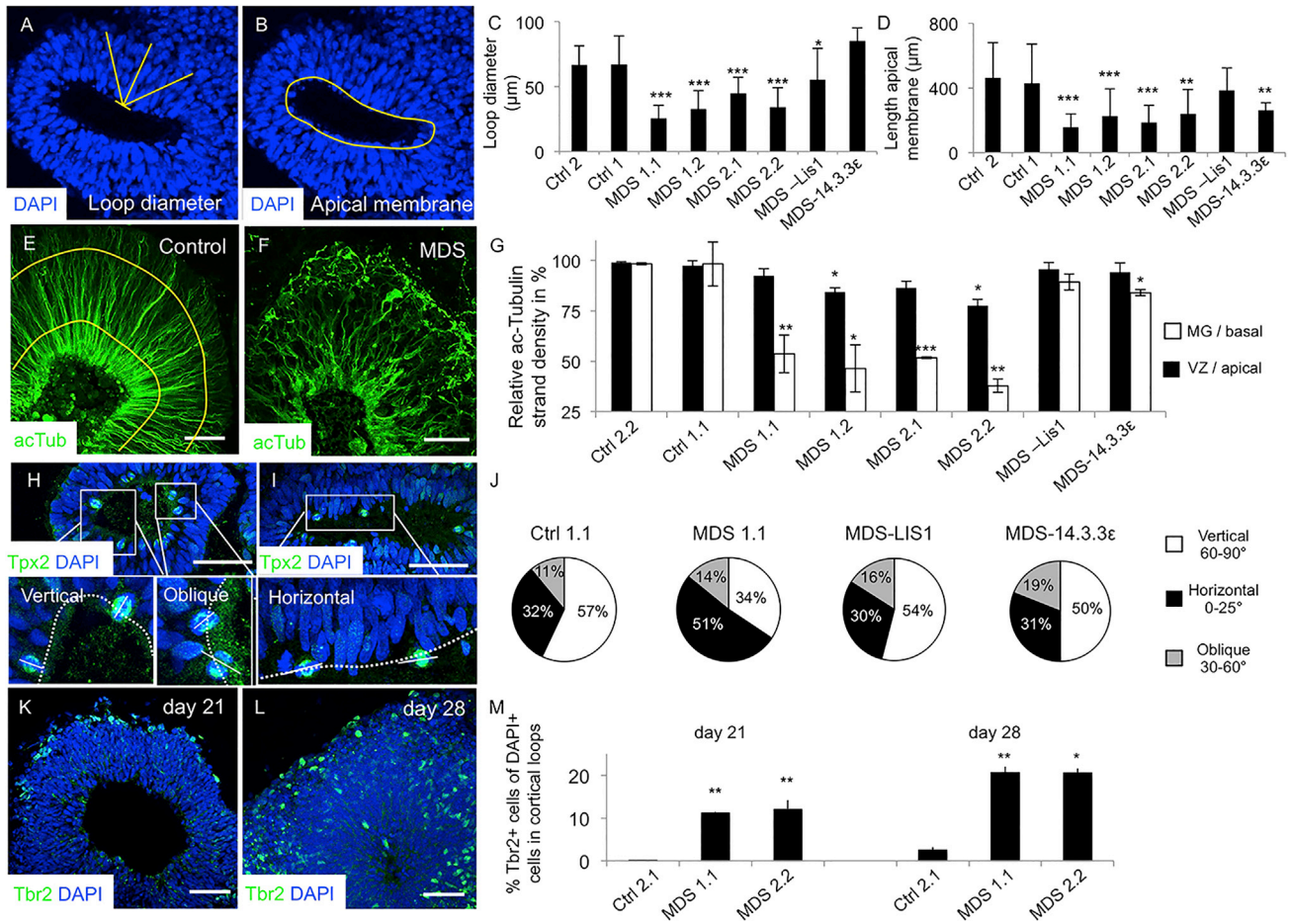


**Figure 2. Altered Microtubule Networks and Increased Neurogenesis in MDS-Derived Organoids**

(A and B) Schematic illustration of how loop diameter (A) and length of apical membrane (B) were quantified.

(C and D) Quantification of the loop diameter (C) and length of apical membrane (D) in control (Ctrl2 n = 42; Ctrl1 n = 24), patient (MDS1.1 n = 29; MDS1.2 n = 27; MDS2.1 n = 29; MDS2.2 n = 10), and the genetic rescue organoids (MDS-LIS1 n = 14; MDS14.3.3ε n = 12). Error bars, ±SD. \*p < 0.05, \*\*p < 0.01, \*\*\*p < 0.001.

(E and F) Immunostaining for acetylated α-tubulin (acTub) in control- (E) and MDS- (F) derived organoids. Scale bars, 50 μm.

(G) Quantification of the ac-tubulin strand density at the apical (VZ) and the basal (MG) side in control (Ctrl2.2 n = 5; Ctrl2.1 n = 8), patient (MDS1.1 n = 13; MDS1.2 n = 5; MDS2.1 n = 5; MDS2.2 n = 10), and rescue organoids (MDS-LIS1 n = 9; MDS-14.3.3ε n = 10). A schematic illustration of the area of measurement (33 percentile VZ/apical, 66 percentile MG/basal) is shown in (E). Error bars, ±SD. \*p ≤ 0.05; \*\*p ≤ 0.01, \*\*\*p ≤ 0.001.

(H and I) Representative images of vertical and oblique (H) as well as horizontal (I) division planes in mitotic vRGCs. Mitotic spindles are stained by Tpx2. Scale bars, 50 μm.

(J) Quantification of the division planes of vRGCs in control (n = 91), MDS (n = 105), MDS-LIS1 (n = 63), and MDS-14.3.3ε (n = 118) organoids at day 20.

(K and L) Representative images of MDS-derived organoids stained with Tbr2 at day 21 (K) and day 28 (L). Scale bars, 50 μm.

(M) Quantification of Tbr2<sup>+</sup> intermediate progenitors (IP) in control- and MDS-derived organoids (at day 21: n > 2,000 cells from a total of n = 6 loops per condition, day 28: n > 1,200 cells from a total of n = 6 loops per condition). Error bars, ±SD. \*p < 0.05, \*\*p < 0.01.

We thus wondered whether we could also observe an increase in oblique spindle orientation in dividing MDS vRGCs by labeling the spindle of mitotic cells with Tpx2 and relating the orientation relative to the VZ-like surface (Figures 2H and 2I). Surprisingly, we found a prominent and significant switch of the spindle orientation from vertical, symmetric toward horizontal, asymmetric cleavage planes (Ctrl1.1: vertical: 57.14%, horizontal: 31.87%, oblique: 11.0%, n = 91; MDS1.1: vertical: 34.29%, horizontal: 51.43%, oblique: 14.23%, n = 105; Figure 2J; Tables S3 and S5), while the number of oblique cleavage planes was not significantly affected. In line with this observation, we found a strong

increase in the number of Tbr2<sup>+</sup> IPs (day 21: Ctrl2.1: <1%; MDS1.1: 11.35% ± 0.15%; MDS2.2: 12.2% ± 1.98%; day 28: Ctrl2.1: 2.64% ± 0.60%; MDS1.1: 20.79% ± 1.22%; MDS2.2: 20.65% ± 0.95%; Figures 2K–2M). Re-expression of LIS1 or 14.3.3ε in MDS cells resulted in a partial restoration of the switch in vRGCs' cleavage plane orientation (MDS-LIS1: vertical: 54.84%, horizontal: 29.84%, oblique: 15.32%, n = 63; MDS-14.3.3ε: vertical: 50.0%, horizontal: 31.51%, oblique: 19.49%, n = 118; Figure 2J; Table S3) and a significant decrease in the number of Tbr2-positive IPs (Figure S4Q; day 28: MDS-LIS1: 11.7% ± 1.28%, MDS-14.3.3ε: 5.36% ± 0.98%). These results

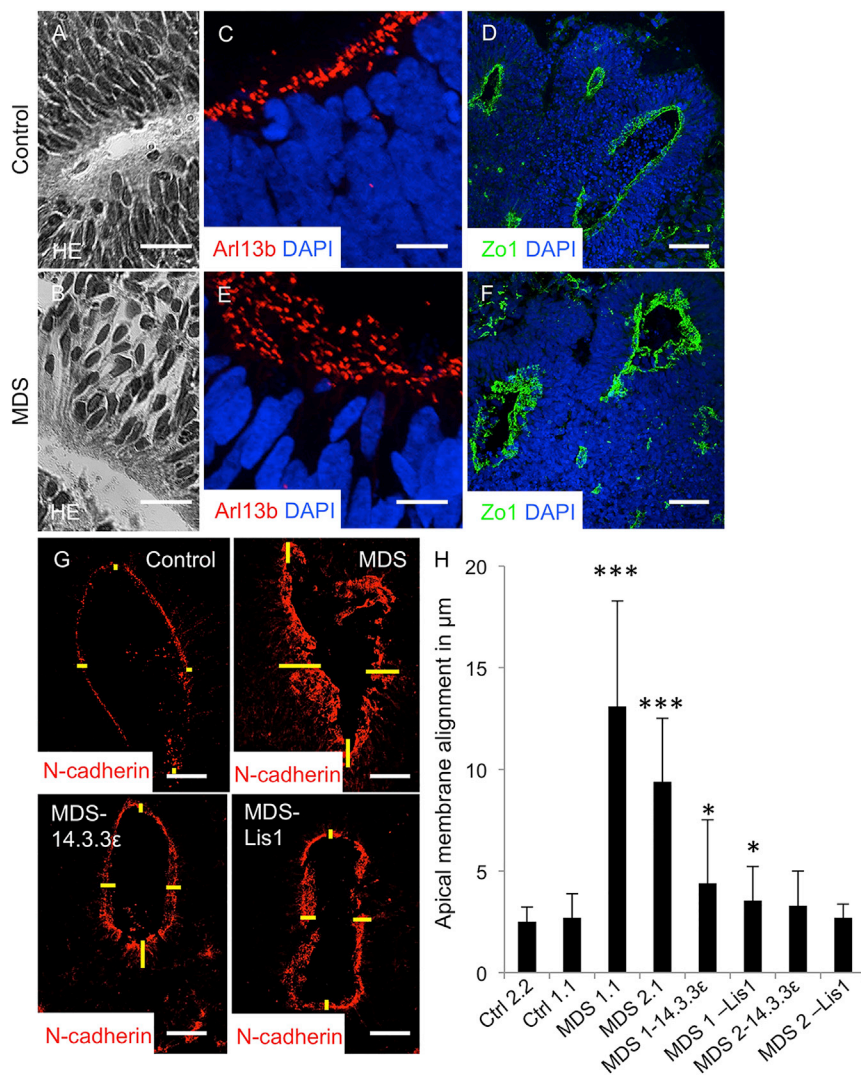


### Figure 3. Disruption of the VZ Niche Architecture in MDS-Derived Organoids

(A and B) H&E staining of the VZ-like area in control- (A) and in MDS- (B) derived organoids. Scale bars, 30  $\mu\text{m}$ .

(C–F) Immunostainings for Arl13b and Zo1 in control- (C and D) and MDS- (E and F) derived organoids. Scale bars, in (C) and (E), 10  $\mu\text{m}$ , and in (D) and (F), 50  $\mu\text{m}$ .

(G) Immunostaining for N-cadherin in control, MDS, MDS-LIS1 rescue, and MDS-14.3.3 $\epsilon$  rescue organoids. Scale bar, 50  $\mu\text{m}$ .

(H) Quantification of the apical membrane alignment in control (Ctrl2.2 n = 16; Ctrl1.1 n = 6), MDS (MDS1.1 n = 23; MDS2.1 n = 15), MDS-LIS1 rescue (MDS1-LIS1 n = 18; MDS2-LIS1 n = 16), and MDS-14.3.3 $\epsilon$  rescue (MDS1-14.3.3 $\epsilon$  n = 14; MDS2-14.3.3 $\epsilon$  n = 15) organoids. A schematic illustration of the area of measurement (yellow lines at 90°, 180°, 270°, and 360°) is shown in (G). Error bars,  $\pm$ SD. \*p  $\leq$  0.05; \*\*p  $\leq$  0.01, \*\*\*p  $\leq$  0.001.

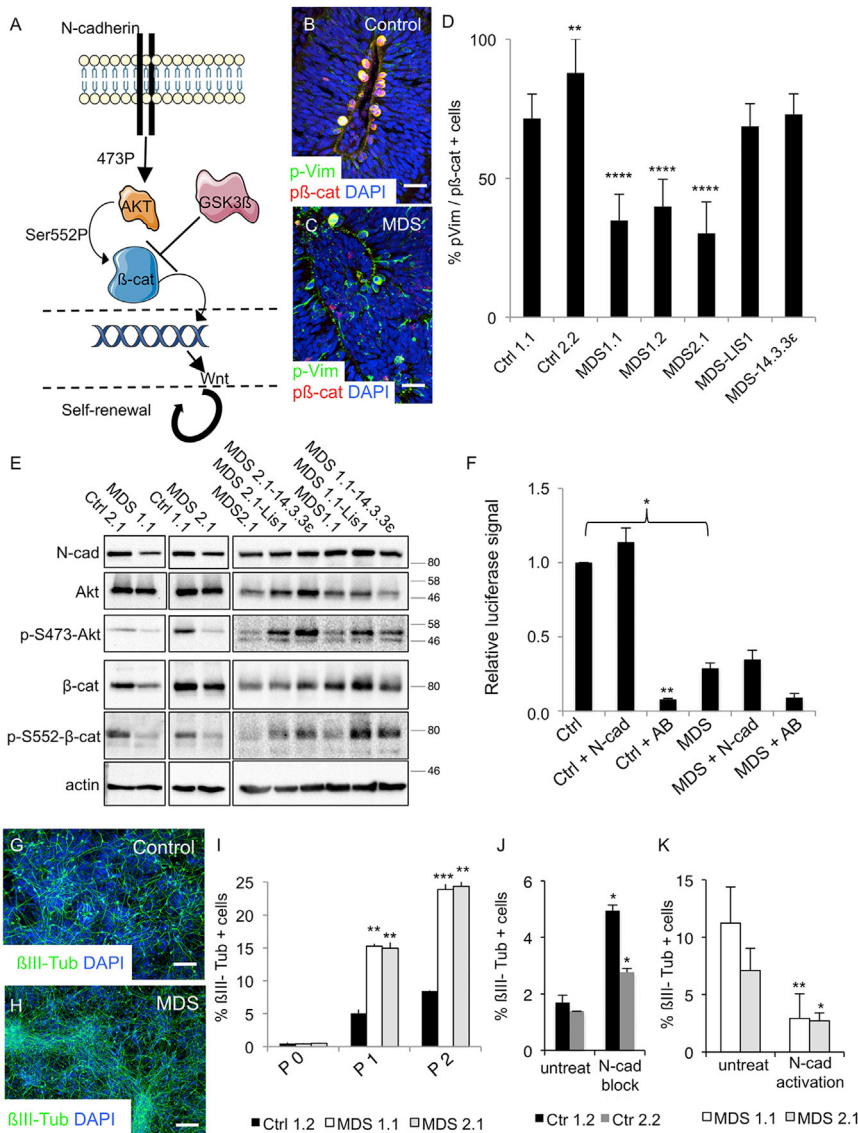
suggest that a transition from symmetric to asymmetric division of vRGCs and an increased generation of fate-restricted IPs at the cost of the stem cell pool might represent the major underlying mechanism for the reduced size and expansion rate of MDS-derived organoids.

### Disruption of the Cortical Niche in MDS-Derived Organoids Results in Alterations of the N-Cadherin/ $\beta$ -Catenin Signaling Axis

The explicit switch in spindle orientation from vertical to horizontal division rather than a randomized increase of oblique cleavage planes suggests that in addition to cell-autonomous defects caused by alterations of the microtubule network other signaling pathways might contribute to the observed phenotype. In this context, adherens junctions have been described to control vRGCs' self-renewal (Marthiens et al., 2010; Stocker and Chenn, 2009), and data from transgenic mouse models have demonstrated that a disruption of the LIS1/NDEL1/14.3.3 $\epsilon$  complex re-

sults in disorganization of vRGCs' lateral cell-cell contacts and irregular expression of apical adhesion molecules (Pawlisz et al., 2008; Pramparo et al., 2011). We thus investigated the organization of the apical ventricular surface in more detail. Indeed, we observed severe alterations in the organization of the ventricular niche in MDS organoids. Whereas vRGCs in control cultures arranged well-organized, stacked, and densely packed perpendicular to the ventricular surface, in MDS organoids vRGC organization was less tight with haphazard positioned cells retracted from the apical membrane (Figures 3A and 3B). This was associated with an indistinct apical lining of cilia along the VZ-like surface in MDS organoids (Figures 3C, 3E, S4E, and S4H). In addition, we found severe alteration in the organization of cell adhesion molecules of the VZ niche. Whereas control organoids exhibited a fine adherent junction belt at the most apical side with accumulation of N-cadherin and zonula occludens protein 1 (Zo1), this organization was significantly altered in MDS-derived cultures without a compact apical distribution (Figures 3D, 3F–3H, S4F, S4G, S4I, and S4J). In MDS-LIS1 and MDS-14.3.3 $\epsilon$  rescue organoids, the organization of the cells within the VZ niche, expression of cell adhesion molecules, and apical membrane alignment was rescued to a stage more similar to control organoids (Figures 3G, 3H, and S4R–S4U). The observed changes in the organization of the VZ niche are also in line with histological data from MDS patients' autopsy brains showing disruption of the neuroepithelium along the VZ surface (Sheen et al., 2006).

We next wondered how the alterations in the organization of the ventricular niche and distribution of adhesion molecules are connected to the reduced organoid size and premature



differentiation phenotype and how the explicit and non-random switch of vRGC division planes might be explained mechanistically. Data from mouse models indicate that active Wnt/β-catenin signaling controls vRGC proliferation (Chenn and Walsh, 2002; Zechner et al., 2003) and that the adhesion molecule N-cadherin is involved in controlling Wnt activity by regulating AKT phosphorylation, which, in turn, phosphorylates β-catenin at serine 552 (p-Ser552-β-catenin) resulting in its stabilization and activation (Zhang et al., 2010, 2013). We thus investigated the phosphorylation state of β-catenin at Ser552 in dividing vRGCs. In control organoids, we observed widespread co-localization of p-Ser552-β-catenin in dividing p-vimentin-positive vRGCs (Ctrl1.1: 71.5% ± 8.78% n = 10; Ctrl2.2: 87.87% ± 12.27% n = 15; Figures 4B and 4D). In contrast, cortical loops from patient-derived organoids exhibited a significantly reduced expression of p-Ser552-β-catenin in p-vimentin-positive vRGCs

(MDS1.1: 34.79% ± 9.41% n = 9; MDS1.2: 39.84% ± 9.76% n = 15; MDS2: 30.21% ± 11.33% n = 9; Figures 4C and 4D). Re-expression of LIS1 or 14.3.3e resulted in a more widespread co-localization of p-Ser552-β-catenin-positive dividing vRGCs at the apical surface (MDS-LIS1: 68.62% ± 8.15% n = 11; MDS-14.3.3e: 71.93% ± 7.41% n = 11; Figure 4D). These data indicate that vRGCs in MDS organoids indeed show an impaired activation of β-catenin and that this might be due to alterations in the N-cadherin/β-catenin signaling axis.

To investigate the interaction between N-cadherin and β-catenin in more detail and to decipher how these two proteins are connected functionally, we became interested in addressing Wnt activity in MDS and control vRGCs and whether manipulation of N-cadherin results in changes of the Wnt activation state. As these experiments are challenging in a 3D organoid system, we wondered whether certain aspects of the observed phenotypes are reflected in high-density 2D cultures consisting of essentially pure vRGCs organized as neural rosettes (Shi et al.,

2012). Indeed, we found that patient-derived rosettes exhibit reduced levels of the proteins involved in the intracellular cascades connecting niche signaling to  $\beta$ -catenin signaling (reduced levels of N-cadherin, phosphorylated AKT at Ser 473,  $\beta$ -catenin phosphorylated at Ser 552 as well as total  $\beta$ -catenin; Figure 4E). These alterations could be attributed to LIS1 and 14.3.3 $\epsilon$  as re-expression of LIS1 or 14.3.3 $\epsilon$  resulted in expression and phosphorylation levels of the proteins more similar to the wild-type situation (Figure 4E).

To further analyze Wnt signaling and the effect of N-cadherin on Wnt activity, we generated Wnt reporter cell lines expressing the pSuper8XTOPFlash luciferase reporter. Indeed, MDS-derived neural rosettes exhibit reduced levels of Wnt reporter activity compared to cells derived from healthy controls (Figure 4F). Interestingly and in line with the proposed mode of interaction, Wnt reporter activity directly depended on N-cadherin function as blocking N-cadherin activity with a N-cadherin blocking antibody resulted in a strong and highly significant decrease in Wnt reporter activity, whereas activating N-cadherin by exposure of the cultures to recombinant N-cadherin protein induced activation of the Wnt reporter (Figure 4F).

We next asked whether manipulation of N-cadherin would directly influence the proliferation and differentiation properties of our cultures. To that end, cortical rosettes were cultured in the absence of any growth factors, and differentiation into neurons was investigated by immunocytochemistry every 5 days. Interestingly, MDS-derived cultures showed a significant increase in the number of neurons over time when compared to cultures derived from healthy controls, indicating that the reduction of Wnt activity leads to premature neurogenesis also in 2D (Figures 4G–4I). Importantly, blocking N-cadherin in control cultures significantly induced differentiation of the cells (Figure 4J), whereas activating N-cadherin in MDS-derived cortical progenitors rescued early neurogenesis (Figure 4K). These data demonstrate that there is indeed a direct link between active N-cadherin signaling and the Wnt pathway. In addition, these data also suggest that this pathway is disrupted in MDS leading to an imbalance of proliferation and differentiation in patient-derived cortical progenitors and that manipulation of N-cadherin results in changes of this balance.

### Phenotypic Alterations in MDS-Derived Organoids Can Be Rescued by Wnt Activation

Based on these results, we tested whether pharmacological activation of  $\beta$ -catenin by inhibition of GSK3 $\beta$  affects the phenotypic alterations observed in MDS patient-derived organoids. Indeed, exposure of the cultures to the GSK3 $\beta$  inhibitor CHIR99021 resulted in much more clear and homogeneous generation of cortical loops compared to the non-treated cultures (Figures 5A and 5B) and a marked rescue of the co-expression of p-Ser552- $\beta$ -catenin in p-vimentin-positive dividing vRGCs (Figure 5C). When investigating the plane of cell division, we observed that exposure to CHIR99021 resulted in a switch of vertical and horizontal division planes in MDS organoids leading to division modes comparable to the healthy control situation (Figures 5D and S5C; Tables S3–S5). This was also reflected when quantifying the parameters at the level of the cortical loops where we observed a significant increase of all parameters

following exposure to the GSK3 $\beta$  inhibitor (depicted are the relative change of all parameters compared to the untreated situation, the loop diameter, and length of the apical membrane; Figures 5E–5G and S5D–S5G). The phenotypic rescue was specific to MDS organoids as neither the plane of cell division nor the individual loop parameters were significantly affected by the exposure to CHIR99021 in control-derived organoids (Figures 5D–5G and S5; Tables S4 and S5). Importantly, the aberrant organization of ventricular niche and expression of cell adhesion molecules was not affected by  $\beta$ -catenin activation, suggesting that these alterations are upstream of  $\beta$ -catenin function (Figures S4K–S4N).

## DISCUSSION

The most prominent histopathological hallmark of LIS1-associated lissencephalies is the disorganization of the cerebral cortex presenting with aberrantly positioned neurons (Francis et al., 2006). This compelled researchers to concentrate on the role of LIS1 in neuronal migration. Indeed, the evolutionary conserved LIS1/NDEL1/14.3.3 $\epsilon$  protein complex has a well-documented function in regulating centrosomal protein localization and microtubule dynamics, both critically involved in nuclear movement and neuronal migration (Moon and Wynshaw-Boris, 2013). An additional and largely neglected phenotype of the disease is that most patients with lissencephaly are either microcephalic or have a borderline low brain size (Allanson et al., 1998). This points toward an additional role of LIS1 in neural progenitor proliferation. And indeed, data from rodents suggest that the LIS1/NDEL1/14.3.3 $\epsilon$  complex plays an important cell-autonomous role in controlling cell division by regulating the plane of the mitotic spindle during mitosis resulting in a random distribution of division planes of dividing neural progenitors (Moon et al., 2014; Pawlisz et al., 2008; Yingling et al., 2008). When we investigated cellular and molecular changes caused by a disruption of the LIS1/NDEL1/14.3.3 $\epsilon$  complex in our organotypic human in vitro model of cortical development, we were able to reproduce the “small-brain” phenotype and changes in the planes of cell division of dividing ventricular RGCs. In our hands, however, division planes appeared not random but presented with a systematic switch from vertical to horizontal division planes, compelling us to consider more global changes in cell signaling pathways participating in the observed phenotype.

Here, we describe a so-far unrecognized mechanism of how a deficiency of the LIS1/NDEL1/14.3.3 $\epsilon$  complex converges into an impairment of brain ventricular niche signaling and cell-fate control. We propose that alterations in the microtubule network of vRGCs lead to a disruption of the architecture of the ventricular niche, which, in turn, results in a non-cell-autonomous disturbance of the N-cadherin/ $\beta$ -catenin/Wnt signaling axis. In line with this hypothesis, we demonstrate an irregular lining and distribution of N-cadherin at the apical surface and provide experimental evidence that N-cadherin is functionally connected to  $\beta$ -catenin/Wnt-signaling and the balance between proliferation and differentiation in vRGCs. Most importantly, external activation of the Wnt pathway results in a phenotypic rescue of the observed expansion defects

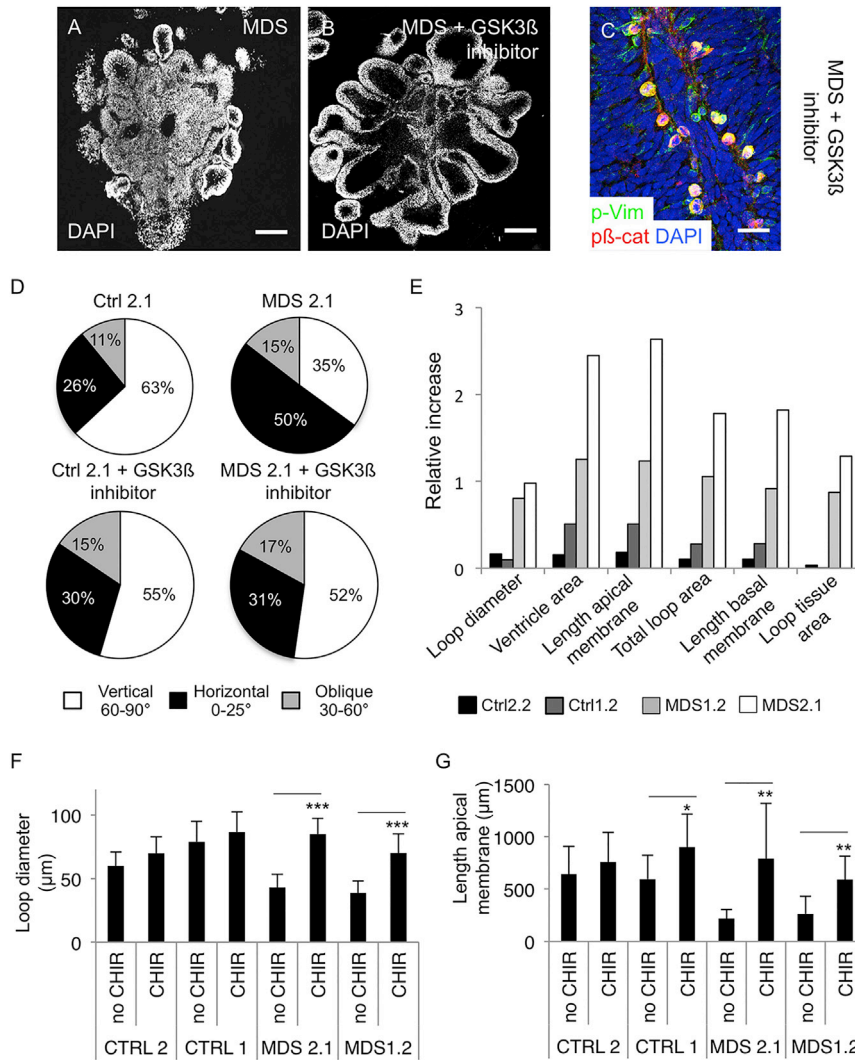


**Figure 5. Activation of  $\beta$ -Catenin/Wnt Signaling Rescues Phenotypic Alterations in MDS-Derived Organoids**

(A and B) Representative images of MDS organoids under standard culture conditions (A) and following exposure to the GSK3 $\beta$  inhibitor CHIR99021 for 10 days (B, depicted are nuclei stained by DAPI). Scale bars, 200  $\mu$ m.

(C) P-Vimentin (p-Vim) and p-Ser552- $\beta$ -catenin (p $\beta$ -cat) immunostaining in MDS-derived organoids treated with the GSK3 $\beta$  inhibitor CHIR99021. Scale bar, 25  $\mu$ m.

(D) Quantification of vertical, horizontal, and oblique division planes of dividing vRGCs in control- and patient-derived organoids in the absence and presence of the GSK3 inhibitor at day 20. Ctrl 1.2 (n = 127), MDS2.1 (n = 115), Ctrl 1.2 + Chir (n = 78), and MDS 2.1 + Chir (n = 88).

(E) Relative change of multiple parameters assessed in cortical neuroepithelial loops of control and patient organoids. Shown is the relative increase in the presence of the GSK3 inhibitor compared to the non-treated control.

(F and G) Quantification of the loop diameter (F) and length of apical membrane (G) in control- and patient-derived organoids in the absence (Ctrl2 n = 10; Ctrl1 n = 9; MDS2.1 n = 8; MDS1.2 n = 8) and the presence of the GSK3 inhibitor (Ctrl2 n = 8; Ctrl1 n = 9; MDS2.1 n = 8; MDS1.2 n = 10). Error bars  $\pm$ SD. \*p < 0.05, \*\*p < 0.01, \*\*\*p < 0.001.

caused by a dysfunction of single genes in a complex tissue environment.

## EXPERIMENTAL PROCEDURES

### Generation of Human iPSCs

Skin fibroblasts were obtained from the Coriell Biorepository (Ctrl1, 2-year-old female, catalog ID GM00969; Ctrl2, 5-month-old male donor, catalog ID GM08680; MDS1, 1-year-old female, catalog ID

GM06097; MDS2, male fetus, 18<sup>th</sup> fetal week, catalog ID GM09208). MDS2 fibroblasts were reprogrammed using retrovirus approach as previously described (Koch et al., 2011). Ctrl1, Ctrl2, and MDS1 fibroblasts were reprogrammed by non-integrative delivery of OCT4, SOX2, KLF4, and c-MYC using Sendai virus (SeV) vectors (Ban et al., 2011). Detailed information on the maintenance of iPSCs, SNP analyses for karyotyping, and germ layer differentiation is provided in the Supplemental Experimental Procedures.

### Generation of LIS1 and 14.3.3e Rescue Lines

Lis1 and 14.3.3e rescue lines were generated by integrating LIS1 or YWHAE into the human AAVS1 locus using plasmids containing the guide RNA (gRNA\_AAVS1-T2, Addgene, catalog no. 41818), the Cas9 (hCas9\_D10A, addgene, catalog no. 41816), and either the PB-TetON-AAVS1-LIS1 or PB-TetON-AAVS1-YWHAE vector. Detailed information on cloning and generation of LIS1 and 14-3-3e rescue cell lines is provided in the Supplemental Experimental Procedures.

### Generation of Brain Organoids

On day 1 of organoid culture, iPSC were dissociated into single cells using TrypLE Express and plated in an ultra-low-binding 96-well plate (6,000–9,000 cells/well, Amsbio, lipidure-coat plate A-U96) in PluriPro (PP) medium (Cell Guidance Systems) supplemented with 50  $\mu$ M ROCK inhibitor Y-27632

specifically in patient-derived organoids. Our observations are in line with another recent study using a similar organoid-based system to investigate changes associated with Miller-Dieker lissencephaly. Without addressing the mechanistic details, they also realized the switch in vRGCs' division planes and an increase in neurogenesis (Bershteyn et al., 2017). Importantly, human brains comprise an additional expanding progenitor population named oRG cells or basal radial glia located in the outer SVZ (Fietz et al., 2010; Hansen et al., 2010) and Bershteyn and colleagues identified changes in cell division (cytokinesis delay) also in this population. The fact that vRGCs in human exhibit a prolonged and more extensive expansion capacity compared to rodents and that rodents exhibit only very few oRGs might in part also explain the decreased phenotypic severity of a disrupted LIS1/NDEL1/14.3.3e complex in mice (Toyo-oka et al., 2003; Yingling et al., 2008). Taken together, our study highlights the potential of organotypic cell-culture models to contribute to an advanced understanding of developmental mechanisms and disease-related changes

(Cell Guidance Systems). Medium was exchanged every other day. At day 5, embryoid bodies (EBs) were transferred to low-adhesion 6-cm plates (Labo-medico) in neural induction media containing DMEM/F12 and Neurobasal (both Gibco and mixed in a 1:1 ratio), N2 supplement (Gibco, 1:200), B27 supplement (Gibco, 1:100), glucose (0.2 mg/mL), 0.5% non-essential amino acids (NEAA, Gibco), heparin (10 µg/mL, Sigma-Aldrich), 1% GlutaMax (Gibco), and the small molecules LDN-193189 (180 nM, Miltenyi Biotec), A83-01 (500 nM, Stemgent), and IWR-1 (10 µg/mL, Enzo Life Sciences). Five days later, small molecules were removed from the medium, and organoids were embedded into Geltrex (GT, Gibco) matrix at day 12 as previously described (Lancaster and Knoblich, 2014). Organoids were further cultured under continuous agitation using a cell-culture shaker with medium changes every 3–4 days until analyzed. When indicated, the GSK3β inhibitor CHIR99021 (1 µM, Miltenyi Biotec) was added to the culture medium. Quantitative assessments were performed on organoids where forebrain identity of neural tube structures was beforehand validated by immunostainings for Sox2, Pax6, Otx2, and Emx1. Detailed information is provided in the [Supplemental Experimental Procedures](#).

#### Generation of iPSC-Derived Cortical Rosettes

Differentiation of iPSC-derived cortical rosettes was performed as described by Shi et al. with slight adaptations (Shi et al., 2012). Detailed information is provided in the [Supplemental Experimental Procedures](#).

#### Generation of Wnt Reporter Lines and Luciferase Assay

Control- (Ctrl1.2) and patient- (MDS1.2) derived iPSCs were lentivirally transduced with a reporter construct expressing luciferase under the control of the Wnt responsive T-cell factor (TCF) promoter element (pSuperTOPflash; Addgene Plasmid #24308). Detailed information on the generation of the reporter lines and the luciferase assay is provided in the [Supplemental Experimental Procedures](#).

#### Histology and Immunofluorescence

Cells were fixed in 4% paraformaldehyde (PFA) for 10 min at room temperature and blocked in blocking solution (10% fetal calf serum [FCS] in PBS). For more detailed information, see [Supplemental Experimental Procedures](#).

Organoids were fixed in 4% PFA for 20 min at room temperature and allowed to sink in 30% sucrose at 4°C overnight before being embedded in 10%/7.5% gelatin/sucrose and cryosectioned at 20–30 µm. Cryosections were stained with H&E or used for immunostaining. For more detailed information, see [Supplemental Experimental Procedures](#).

#### Immunoblot

Cortical rosettes were harvested for immunoblot analysis 3–4 days following replating. Detailed information is provided in the [Supplemental Experimental Procedures](#).

#### RT-PCR Analysis

RT-PCR was performed in triplicates using biological duplicates. For detailed information, see [Supplemental Experimental Procedures](#).

#### Statistical Analyses

Quantitative data were generated at least in biological triplicates. No statistical methods were used to pre-determine sample sizes, but our sample sizes are similar to those generally employed in the field. All data were collected and processed randomly. Means and SD were computed. All results presented as bar graphs show mean ± SD. Two-sided one-way ANOVA test using Prism 6 software, two-proportion z-test, or Kruskal-Wallis test followed by Bonferroni-corrected pairwise comparisons using a Mann-Whitney U test was performed to determine whether a significant difference exists between groups.

#### SUPPLEMENTAL INFORMATION

Supplemental Information includes Supplemental Experimental Procedures, five figures, and five tables and can be found with this article online at <http://dx.doi.org/10.1016/j.celrep.2017.03.047>.

#### AUTHOR CONTRIBUTIONS

Conceptualization, P.K. and J.L.; Methodology, V.I., G.M., O.K., A.J., K.W., B.B., F.-J.M., and J.L.; Validation, V.I., G.M.; O.K., A.J., K.W., F.M., and R.W.; Formal Analysis, V.I., G.M., O.K., A.J., K.W., F.M., and J.L.; Investigation, V.I., G.M., O.K., A.J., K.W., F.M., R.W., and J.L.; Resources, B.B. and F.-J.M.; Writing – Original Draft, J.L.; Writing – Reviewing & Editing, P.K. and J.L.; Visualization, J.L.; Supervision, P.K. and J.L.; Project Administration, J.L.; Funding Acquisition, J.L.

#### ACKNOWLEDGMENTS

We thank D. Kühne for technical support and Linheng Li, Mark Hembree, and John Pery (Stowers Institute) for kindly providing the anti-p-Ser552-β-catenin antibody. The work was supported by the Ministry of Innovation Science and Research of North Rhine-Westphalia (Junior Research Group, to J.L.), by the University of Bonn BONFOR Program (to J.L.), the ERA-NET NEURON, JTC 2015 Neurodevelopmental Disorders, STEM-MCD (to J.L.), and the German Research Foundation (grant MU 3231/3-1 to F.-J.M.).

Received: July 11, 2016

Revised: January 25, 2017

Accepted: March 13, 2017

Published: April 4, 2017

#### REFERENCES

- Allanson, J.E., Ledbetter, D.H., and Dobyns, W.B. (1998). Classical lissencephaly syndromes: does the face reflect the brain? *J. Med. Genet.* **35**, 920–923.
- Ban, H., Nishishita, N., Fusaki, N., Tabata, T., Saeki, K., Shikamura, M., Takada, N., Inoue, M., Hasegawa, M., Kawamata, S., and Nishikawa, S. (2011). Efficient generation of transgene-free human induced pluripotent stem cells (iPSCs) by temperature-sensitive Sendai virus vectors. *Proc. Natl. Acad. Sci. USA* **108**, 14234–14239.
- Bershteyn, M., Nowakowski, T.J., Pollen, A.A., Di Lullo, E., Nene, A., Wynshaw-Boris, A., and Kriegstein, A.R. (2017). Human iPSC-derived cerebral organoids model cellular features of lissencephaly and reveal prolonged mitosis of outer radial glia. *Cell Stem Cell*, Published online January 9, 2017. <http://dx.doi.org/10.1016/j.stem.2016.12.007>.
- Bi, W., Sapir, T., Shchelochkov, O.A., Zhang, F., Withers, M.A., Hunter, J.V., Levy, T., Shinder, V., Peiffer, D.A., Gunderson, K.L., et al. (2009). Increased LIS1 expression affects human and mouse brain development. *Nat. Genet.* **41**, 168–177.
- Camp, J.G., Badsha, F., Florio, M., Kanton, S., Gerber, T., Wilsch-Bräuninger, M., Lewitus, E., Sykes, A., Hevers, W., Lancaster, M., et al. (2015). Human cerebral organoids recapitulate gene expression programs of fetal neocortex development. *Proc. Natl. Acad. Sci. USA* **112**, 15672–15677.
- Chenn, A., and Walsh, C.A. (2002). Regulation of cerebral cortical size by control of cell cycle exit in neural precursors. *Science* **297**, 365–369.
- Fietz, S.A., Kelava, I., Vogt, J., Wilsch-Bräuninger, M., Stenzel, D., Fish, J.L., Corbeil, D., Riehn, A., Distler, W., Nitsch, R., and Huttner, W.B. (2010). OSVZ progenitors of human and ferret neocortex are epithelial-like and expand by integrin signaling. *Nat. Neurosci.* **13**, 690–699.
- Francis, F., Meyer, G., Fallet-Bianco, C., Moreno, S., Kappeler, C., Socorro, A.C., Tuy, F.P., Beldjord, C., and Chelly, J. (2006). Human disorders of cortical development: from past to present. *Eur. J. Neurosci.* **23**, 877–893.
- Hansen, D.V., Lui, J.H., Parker, P.R., and Kriegstein, A.R. (2010). Neurogenic radial glia in the outer subventricular zone of human neocortex. *Nature* **464**, 554–561.
- Kadoshima, T., Sakaguchi, H., Nakano, T., Soen, M., Ando, S., Eiraku, M., and Sasai, Y. (2013). Self-organization of axial polarity, inside-out layer pattern, and species-specific progenitor dynamics in human ES cell-derived neocortex. *Proc. Natl. Acad. Sci. USA* **110**, 20284–20289.
- Kato, M., and Dobyns, W.B. (2003). Lissencephaly and the molecular basis of neuronal migration. *Hum. Mol. Genet.* **12**, R89–R96.

- Koch, P., Breuer, P., Peitz, M., Jungverdorben, J., Kesavan, J., Poppe, D., Doerr, J., Ladewig, J., Mertens, J., Tüting, T., et al. (2011). Excitation-induced ataxin-3 aggregation in neurons from patients with Machado-Joseph disease. *Nature* *480*, 543–546.
- Lancaster, M.A., and Knoblich, J.A. (2014). Generation of cerebral organoids from human pluripotent stem cells. *Nat. Protoc.* *9*, 2329–2340.
- Lancaster, M.A., Renner, M., Martin, C.A., Wenzel, D., Bicknell, L.S., Hurles, M.E., Homfray, T., Penninger, J.M., Jackson, A.P., and Knoblich, J.A. (2013). Cerebral organoids model human brain development and microcephaly. *Nature* *501*, 373–379.
- Mariani, J., Coppola, G., Zhang, P., Abyzov, A., Provini, L., Tomasini, L., Amenduni, M., Szekely, A., Palejev, D., Wilson, M., et al. (2015). FOXG1-dependent dysregulation of GABA/glutamate neuron differentiation in autism spectrum disorders. *Cell* *162*, 375–390.
- Marthiens, V., Kazanis, I., Moss, L., Long, K., and French-Constant, C. (2010). Adhesion molecules in the stem cell niche—more than just staying in shape? *J. Cell Sci.* *123*, 1613–1622.
- Moon, H.M., and Wynshaw-Boris, A. (2013). Cytoskeleton in action: Lissencephaly, a neuronal migration disorder. *Wiley Interdiscip. Rev. Dev. Biol.* *2*, 229–245.
- Moon, H.M., Youn, Y.H., Pemble, H., Yingling, J., Wittmann, T., and Wynshaw-Boris, A. (2014). LIS1 controls mitosis and mitotic spindle organization via the LIS1-NDEL1-dynein complex. *Hum. Mol. Genet.* *23*, 449–466.
- Pawlisz, A.S., Mutch, C., Wynshaw-Boris, A., Chenn, A., Walsh, C.A., and Feng, Y. (2008). Lis1-Nde1-dependent neuronal fate control determines cerebral cortical size and lamination. *Hum. Mol. Genet.* *17*, 2441–2455.
- Pramparo, T., Libiger, O., Jain, S., Li, H., Youn, Y.H., Hirotsune, S., Schork, N.J., and Wynshaw-Boris, A. (2011). Global developmental gene expression and pathway analysis of normal brain development and mouse models of human neuronal migration defects. *PLoS Genet.* *7*, e1001331.
- Qian, X., Nguyen, H.N., Song, M.M., Hadiono, C., Ogden, S.C., Hammack, C., Yao, B., Hamersky, G.R., Jacob, F., Zhong, C., et al. (2016). Brain-region-specific organoids using mini-bioreactors for modeling ZIKV exposure. *Cell* *165*, 1238–1254.
- Sheen, V.L., Ferland, R.J., Neal, J., Harney, M., Hill, R.S., Banham, A., Brown, P., Chenn, A., Corbo, J., Hecht, J., et al. (2006). Neocortical neuronal arrangement in Miller Dieker syndrome. *Acta Neuropathol.* *111*, 489–496.
- Shi, Y., Kirwan, P., Smith, J., Robinson, H.P., and Livesey, F.J. (2012). Human cerebral cortex development from pluripotent stem cells to functional excitatory synapses. *Nat. Neurosci.* *15*, 477–486.
- Stocker, A.M., and Chenn, A. (2009). Focal reduction of alphaE-catenin causes premature differentiation and reduction of beta-catenin signaling during cortical development. *Dev. Biol.* *328*, 66–77.
- Toyo-oka, K., Shionoya, A., Gambello, M.J., Cardoso, C., Leventer, R., Ward, H.L., Ayala, R., Tsai, L.H., Dobyns, W., Ledbetter, D., et al. (2003). 14-3-3epsilon is important for neuronal migration by binding to NUDEL: a molecular explanation for Miller-Dieker syndrome. *Nat. Genet.* *34*, 274–285.
- Tsai, J.W., Chen, Y., Kriegstein, A.R., and Vallee, R.B. (2005). LIS1 RNA interference blocks neural stem cell division, morphogenesis, and motility at multiple stages. *J. Cell Biol.* *170*, 935–945.
- Wynshaw-Boris, A. (2007). Lissencephaly and LIS1: Insights into the molecular mechanisms of neuronal migration and development. *Clin. Genet.* *72*, 296–304.
- Yingling, J., Youn, Y.H., Darling, D., Toyo-Oka, K., Pramparo, T., Hirotsune, S., and Wynshaw-Boris, A. (2008). Neuroepithelial stem cell proliferation requires LIS1 for precise spindle orientation and symmetric division. *Cell* *132*, 474–486.
- Zechner, D., Fujita, Y., Hülsken, J., Müller, T., Walther, I., Taketo, M.M., Crenshaw, E.B., 3rd, Birchmeier, W., and Birchmeier, C. (2003). beta-Catenin signals regulate cell growth and the balance between progenitor cell expansion and differentiation in the nervous system. *Dev. Biol.* *258*, 406–418.
- Zhang, J., Woodhead, G.J., Swaminathan, S.K., Noles, S.R., McQuinn, E.R., Pisarek, A.J., Stocker, A.M., Mutch, C.A., Funatsu, N., and Chenn, A. (2010). Cortical neural precursors inhibit their own differentiation via N-cadherin maintenance of beta-catenin signaling. *Dev. Cell* *18*, 472–479.
- Zhang, J., Shemezis, J.R., McQuinn, E.R., Wang, J., Sverdlov, M., and Chenn, A. (2013). AKT activation by N-cadherin regulates beta-catenin signaling and neuronal differentiation during cortical development. *Neural Dev.* *8*, 7.